

LETTER TO THE EDITOR

Cosmic-ray electrons and the magnetic field of the North Polar Spur

Guobin Mou¹, Jianhao Wu^{2,3}, and Yoshiaki Sofue⁴

¹ Department of Astronomy, School of Physics and Technology, Wuhan University, Wuhan 430072, China
e-mail: gbmou@whu.edu.cn

² Department of Physics and Institute of Theoretical Physics, The Chinese University of Hong Kong, Shatin, Hong Kong SAR, China
e-mail: jianhao.wu@link.cuhk.edu.hk

³ School of Computer Science, Wuhan University, Wuhan 430072, China

⁴ Institute of Astronomy, The University of Tokyo, Mitaka, Tokyo 181-0015, Japan

ABSTRACT

Aims. The recent confirmation of the bipolarity of the eROSITA bubbles suggests that the well-known North Polar Spur (NPS)/Loop I probably is a 10 kpc sized relic in the Galactic halo and not a small local structure near the Sun. By virtue of multiwavelength observations of the NPS, unprecedentedly precise parameter constraints on the cosmic-ray electrons (CRe) and magnetic field in the post-shock halo medium can be provided.

Methods. The parameters of the CRe and the magnetic field can be derived independently by modeling the gamma-ray and the radio data of the NPS via inverse Compton scattering and synchrotron emission, respectively.

Results. Our main results are (1) that the energy density of the CRe is $(3-6)\times 10^{-14}$ erg cm⁻³, and the spectral index is $p \approx 2.0 \pm 0.1$, below the cooling break energy of about 5 GeV; (2) that the magnetic field strength is 3 μ G; and (3) that the shock acceleration efficiency of the CRe is (1-2)%. Given the Mach number of 1.5, the high acceleration efficiency and flat spectrum of the CRe suggest that preexisting relativistic electrons may be reaccelerated in the NPS. Alternatively, these CRe could be accelerated by an evolving shock in the early epoch when its Mach number is high, and efficiently diffuse throughout the post-shock halo gas. In addition, the cooling break energy suggests that the cooling timescale is 10⁷ yr, which agrees with the age of the eROSITA bubbles.

Key words. acceleration of particles – radiation mechanisms: non-thermal – ISM: jets and outflows – Galaxy: halo – shock waves

1. Introduction

Loop I, the giant loop spanning almost 100 degrees in the radio sky map, has been known for 60 years (Large et al. 1962). Its eastern part is prominently brighter than its western part, and it is called the North Polar Spur (NPS). Loop I/NPS is outstanding in a wide range of frequencies from tens of MHz to tens of GHz (e.g., De Oliveira-Costa et al. 2008), and the lower frequencies of $\lesssim 10^1$ GHz are thought to be dominated by synchrotron emission. Moreover, it is also visible in the X-ray (Snowden et al. 1997) and gamma-ray band (Casajjian & Grenier 2009; Su et al. 2010). During the past decades, most works have regarded the Loop I/NPS as a local structure (LS) of $\sim 10^2$ parsecs that could originate from an old supernova remnant (SNR) or stellar activity (Weaver 1979; Wolleben 2007). A recent work (Panopoulou et al. 2021) investigated the optical polarization angles of nearby stars induced by foreground dust (Das et al. 2020). The starlight polarization angles at Galactic latitude $b > 30^\circ$ are essentially aligned with that of the radio NPS in tens of GHz, and based on this, Panopoulou and collaborators argued that this part of the NPS should be located within ~ 100 pc.

Nevertheless, Sofue thought that it could be a large halo structure (HS) of about 10 kpc at the Galactic center distance (Sofue 1977, 2000; Sofue et al. 2016) that might have originated from a past outburst of the Galactic center. This scenario is becoming attractive because it is consistent with the multiwavelength structures revealed in the recent decade, including their southern counterparts in the X-ray band (Predehl et al. 2020),

the Fermi bubbles (Su et al. 2010), and the polarized radio lobes (Carretti et al. 2013). In particular, the discovery of the southern eROSITA bubble provides compelling evidence that supports the HS picture, which is also supported by foreground absorption in the X-rays by the Aquila Rift clouds at a distance of 1 kpc (Sofue 2015; Sofue et al. 2016). The NPS-like structure in the soft X-ray band is also reproduced in hydrodynamic simulations modeling the Fermi bubbles (Guo & Mathews 2012; Mou et al. 2014; Sarkar 2019). Because they overlap much, radio Loop I and the northern eROSITA bubble are probably the same physical structure, the radio emission of which probably come froms the synchrotron radiation of cosmic ray electrons (CRe) accelerated by the forward shock. The radio and X-ray NPS probably is a galactic center (GC)–distance halo structure, while it coincidentally overlaps with the foreground local dust and H I (Das et al. 2020). As shown in our recent simulation study (Mou et al. 2023), both the prominent east–west asymmetry of the Loop I/NPS and the faintness of its southern counterpart (north–south asymmetry), which are frequently quoted as support for the LS scenario, could be caused by a crossing CGM wind injected east by north in Galactic coordinates with a velocity of ~ 200 km s⁻¹ (see also Mou et al. 2018; Sofue 2019 for analytical studies). As inferred from X-rays, the Mach number of the Loop I/NPS is ~ 1.5 (corresponding to a shock velocity of 300 km s⁻¹; Kataoka et al. 2013), and the age of the Loop I/NPS probably is 10⁷ yr. In this context, the Loop I/NPS, which possibly has been misinterpreted for several decades, could be an excellent object for

arXiv:2212.04306v3 [astro-ph.HE] 19 Jul 2023

studying the physics of cosmic ray electrons and the magnetic field, and the particle acceleration of shocks and diffusion of CR on the galactic scale. The model and result are presented in Section 2, and we discuss the results in Section 3.

2. Model and result

2.1. Basic method

For the radio NPS (see Figure 1 for the 408 MHz map), our analysis is restricted to the latitude $b > 30^\circ$ to avoid complications near the Galactic plane, which is also in line with the sky region for the gamma-ray data in Jóhannesson & Porter (2021). The temperature spectral index β ($T_B \sim \nu^{-\beta}$) of the NPS is ~ 2.55 between 45 MHz and 408 MHz (Guzmán et al. 2011). It steepens as the frequency increases to GHz: $\beta \sim 2.8$ between 408 MHz and 2.3 GHz (Platania et al. 2003), and ~ 3.0 between 408 MHz and 23 GHz (Miville-Deschênes et al. 2008). Vidal et al. (2015) found that β of the NPS is about 3 between 23 and 41 GHz from WMAP data, but the dispersion is large, and Jew & Grumitt (2020) found it to be $3 - 3.2$ between 30 and 44 GHz from Planck data. The steepening of the synchrotron spectrum suggests a turning point at $\sim 10^0$ GHz, which is indicative of a cooling break in the CRE population. The main cooling mechanisms of CRes in the NPS involve synchrotron and inverse Compton scattering (ICS), which cause the spectral energy distribution (SED) of CRes to steepen by one power of γ_e for the continuous injection case. Here we assumed an SED of CRes to account for the NPS in a broken power-law form with the exponential cutoff at γ_{ct} ,

$$\frac{dN_{cre}}{d\gamma_e} = \begin{cases} N_0 \gamma_e^{-p} & (\gamma_e < \gamma_{br}) \\ N_1 \gamma_e^{-p-1} \exp(-\gamma_e/\gamma_{ct}) & (\gamma_e \geq \gamma_{br}) \end{cases}, \quad (1)$$

where γ_{br} is the Lorentz factor of the cooling break energy E_{br} . Continuity requires $N_1 = N_0 \gamma_{br}$. We investigated the cases with $p = 1.9 - 2.2$, and set the exponential cutoff at $\gamma_{ct} = 9.8 \times 10^5$ (0.5 TeV) for $p \leq 2.0$ and 1.96×10^6 (1 TeV) for $p \geq 2.1$ to improve the fitting of the gamma-ray spectrum. For nonrelativistic bulk motion, which is the case here, the energy distribution peaks at $\gamma_e \sim 2$ because the CRes follow a power-law distribution in momentum (instead of energy) with slope p (Bell 1978; Sironi et al. 2013). Therefore, the SED of CRes (equation 1) can be regarded as starting from $\gamma_e = 2$ ¹. The only two unknown parameters of the CRE population are N_0 and γ_{br} (E_{br}) in equation 1.

We adopted one-zone assumption for simplicity. Because the energy density of the CRes and the magnetic field are coupled, these parameters cannot be derived from radio data alone. Thanks to the Fermi-LAT, the gamma-ray spectrum of the NPS was obtained (e.g., Jóhannesson & Porter 2021). The parameters of CRes can be solved independently via fitting the gamma-ray spectrum through ICS of CRE. After this, the magnetic field strength can be derived by fitting the radio spectrum. This is the basic method of this work.

2.2. Geometry structure

The physical structure of Loop I/NPS is generally regarded as the post-shock medium. Before modeling the radio and gamma-ray NPS, we need to know the thickness of the radiative shell along the sightline – $D_s(l, b)$, where l/b is the Galactic longitude/latitude. We adopted 3D Cartesian coordinates, in which

¹ When the lower bound of $\gamma_e = 1$ or 2 with $p \leq 2.2$ is adopted, the difference in the energy density of the CRes is only a few percent.

the Z-axis is the Galactic polar axis, and the Solar System is located at $(X, Y, Z) = (0, -8.2 \text{ kpc}, 0)$ (Bland-Hawthorn & Gerhard 2016). We constructed a 3D hollow and thick-shelled bubble in the Galactic halo with its center at $(X_{cnt}, 0, Z_{cnt})$. The inner and outer radii of the shell are R_{in} and R_{out} , respectively, in which we forced $R_{in} = Z_{cnt}$ to reduce the degrees of freedom. By testing a series of parameter groups, the four parameters can be estimated by comparing the shell projection in the Galactic coordinates and the observed NPS. The fitting result is $(R_{in}, R_{out}) = (5.0 \text{ kpc}, 7.5 \text{ kpc})$ and $(X_{cnt}, Z_{cnt}) = (1.5 \text{ kpc}, 5.0 \text{ kpc})$, and the modeled $D_s(l, b)$ is shown in Figure 1. The value of $D_s(l, b)$ depends on the specific direction, but is basically in the range of 6–10 kpc (Figure 1c). We adopted $D_s(l, b) = 8 \text{ kpc}$ as the fiducial value. For the LS scenario, when the center is 100 pc from the Sun, the projected thickness of the shell can be obtained by $D_s^{LS} = D_s \cdot (100 \text{ pc} / 9.4 \text{ kpc}) = 0.011 D_s = 0.088 \text{ kpc}$ with the help of similar geometry. Thus, the values of the projected thickness under the two physical scenarios differ by two orders of magnitude, which has a significant impact on the parameters of the CRes that are required to fit the observations.

2.3. Gamma-ray NPS

There are two possible origins for gamma rays: ICS of the interstellar radiation field (ISRF) by CRes, or a hadronic origin (pp collisions). If it is the hadronic origin, the gamma-ray luminosity per unit volume is $j_\gamma \sim f \sigma_{pp} e_{crp} n_{gas} c$, where $f \sim 0.17$ is the fraction of cosmic-ray protons (CRps) kinetic energy transferred into π^0 , which instantaneously decays into gamma rays, $\sigma_{pp} \sim 30 \text{ mb}$ is the cross section of inelastic collision (Aharonian 2004), and e_{crp} is the energy density of CRp. X-ray observations suggest that the density and temperature of the hot gas in the NPS are $n_{gas} \sim (3 - 4) \times 10^{-3} \text{ cm}^{-3}$ and 0.3 keV, respectively (Kataoka et al. 2013, 2015). If we had taken the thermal energy density of the ions as the upper limit of e_{crp} , we would have a gamma-ray intensity of $J_\gamma = (4\pi)^{-1} j_\gamma D_s < 1 \times 10^3 \text{ eV cm}^{-2} \text{ s}^{-1} \text{ sr}^{-1}$, the upper limit of which is about half of the observed value (Jóhannesson & Porter 2021). Thus, a hadronic origin requires relatively extreme conditions in which the energy density of CRp could exceed that of thermal ions, and the gamma rays of the NPS more likely come from ICS.

In ICS, the rate of gamma-ray production per unit volume per unit energy is given by

$$\frac{dn_\gamma(E_\gamma)}{dE_\gamma} = c \int_{\gamma_e} \int_{E_{ph}} \frac{d\sigma_{IC}(E_\gamma, E_e, E_{ph})}{dE_\gamma} \frac{dN_{cre}}{d\gamma_e} d\gamma_e \frac{dn_{ph}}{dE_{ph}} dE_{ph}, \quad (2)$$

where $dN_{cre}/d\gamma_e$ is the energy distribution of the primary CRes (see equation 1), dn_{ph}/dE_{ph} is the number density of an interstellar radiation field (ISRF) photon per unit energy. The differential cross sections of ICS in this equation can be approximated by $d\sigma_{IC}/dE_\gamma = 3\sigma_T (E_e \Gamma_e)^{-1} [2q \ln q + (1 + 2q)(1 - q) + (\Gamma_e q)^2 (1 - q)(2 + 2\Gamma_e q)^{-1}]$, where σ_T is the Thomson cross section, $\Gamma_e \equiv 4E_{ph} E_e / (m_e^2 c^4)$, and $q \equiv E_\gamma \Gamma_e^{-1} (E_e - E_\gamma)^{-1}$ (Blumenthal & Gould 1970). The gamma-ray flux is found from the source term (equation 2) as a sightline integral,

$$\frac{dN_\gamma}{dE_\gamma} = \frac{1}{4\pi} \int \frac{dn_\gamma}{dE_\gamma} dR. \quad (3)$$

The ISRF takes the values in GALPROP² v54 (see Figure A1, Moskalenko et al. 2006; Porter et al. 2006). The line of sight

² <http://galprop.stanford.edu>

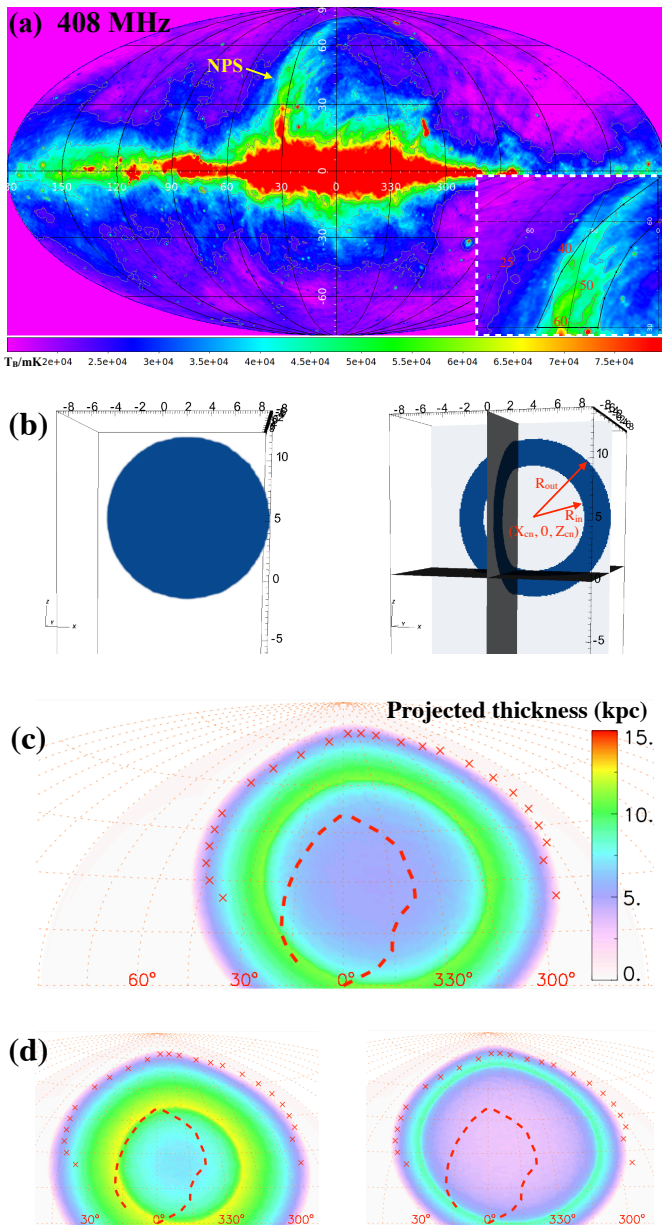


Fig. 1. Observed NPS in the radio band and its geometry model. Panel (a) shows the 408 MHz sky map (Haslam et al. 1982, T_B in mK). The gray contours indicate $T_B = 25$ K, 40 K, 50 K, and 60 K. The right window shows the zoom-in view of the NPS, and the polygon marks the region for radio intensity statistics (similar to the region for gamma-ray analysis in Jóhannesson & Porter 2021). Panel (b) shows the 3D view and the three-slice view of the shell (coordinate values are in units of kpc). Panel (c) shows the projected thickness (D_s) of the radiative shell, accounting for the Loop I/NPS in Galactic coordinates with $(R_{in}, R_{out}) = (5.0$ kpc, 7.5 kpc). The crosses and the dashed line mark the outlines of Loop I and the northern Fermi bubble, respectively (see Su et al. 2010 for the coordinates). Panel (d) show the projected thickness maps for $(R_{in}, R_{out}) = (4.0$ kpc, 7.5 kpc) (left) and $(6.0$ kpc, 7.5 kpc) (right).

toward the NPS passes through different regions with different ISRFs. We took the ISRF at $(R, z) = (5$ kpc, 5 kpc) as the seed photon (R is the galactocentric distance, and z is the height from the midplane of the Galactic disk).

Table 1. Parameters for modeling the radio and gamma-ray NPS. A Y or N (yes or no) after the E_{br} -value indicates whether the values of the modeled $\bar{\alpha}_1$ and $\bar{\alpha}_2$ meet the radio-fit conditions, and LS after the p -value marks the local structure scenario.

p	E_{br} GeV	N_0 cm^{-3}	e_{cre} erg cm^{-3}	B μG	$\bar{\alpha}_1$	$\bar{\alpha}_2$
1.9	3.5 (Y)	2.7×10^{-9}	3.4×10^{-14}	3.4	-0.57	-0.91
2.0	4 (N)	7.8×10^{-9}	5.6×10^{-14}	2.9	-0.61	-0.95
2.0	5 (Y)	6.3×10^{-9}	4.6×10^{-14}	3.2	-0.57	-0.91
2.0	6 (N)	5.2×10^{-9}	3.9×10^{-14}	3.4	-0.55	-0.87
2.1	6 (Y)	1.4×10^{-8}	6.0×10^{-14}	3.3	-0.60	-0.91
2.2	8 (N)	3.4×10^{-8}	9.5×10^{-14}	3.2	-0.63	-0.89
1.9LS	3 (Y)	1.8×10^{-7}	2.3×10^{-12}	4.1	-0.59	-0.91
2.0LS	4 (Y)	4.7×10^{-7}	3.4×10^{-12}	3.7	-0.59	-0.93
2.1LS	5 (Y)	9.9×10^{-7}	4.3×10^{-12}	3.9	-0.60	-0.93
2.2LS	8 (N)	2.1×10^{-6}	5.8×10^{-12}	4.0	-0.62	-0.87

2.4. Radio NPS

For the radio NPS (Figure 1a), we selected a similar region to the one used in the gamma-ray analysis (Jóhannesson & Porter 2021), and simply chose the region of longitude $l = 60^\circ$ (outside and close to the NPS) as the radio background or foreground, of which $T_B \sim 22$ K at 408 MHz. Subtracting the background or foreground of the same latitudes, we derived that the average brightness temperature of the NPS at 408 MHz is $T_B \approx 20$ K. By fitting the gamma-ray spectrum, we obtained a series of possible distributions of the CRe with different E_{br} and N_0 . For each SED, we then calculated the synchrotron emission with different magnetic field strengths, in which the pitch angle between the electron velocity and the field was assumed to be random. We defined the radio-fit conditions as follows: matching the intensity at 408 MHz, spectral indices of $\bar{\alpha}_1 = -0.55 \sim -0.60$ (45–408 MHz), and $\bar{\alpha}_2 = -1.0 \pm 0.1$ (0.408–23 GHz), in which $\bar{\alpha}_1 \equiv \ln(S_{45\text{MHz}}/S_{408\text{MHz}})/\ln(45/408)$ and $\bar{\alpha}_2 \equiv \ln(S_{408\text{MHz}}/S_{23\text{GHz}})/\ln(0.408/23)$. These conditions restrict the model parameters to a narrow range.

2.5. Results

We modeled the radio and gamma-ray data with the setup with $p = 2.0$ and $E_{br} = 5$ GeV as the fiducial case (Table 1 and Figure 2). The coefficients of the CRe SED (equation 1) in the fiducial case were $N_0 = 6.3 \times 10^{-9} \text{ cm}^{-3}$ and $N_1 = 6.2 \times 10^{-5} \text{ cm}^{-3}$. The energy density of the CRes is thus $e_{cre} = 4.6 \times 10^{-14} \text{ erg cm}^{-3}$, and the number density of the CRes ($\gamma_e \geq 2$) is $3.3 \times 10^{-9} \text{ cm}^{-3}$, which is 10^{-6} of the thermal density derived from X-ray observations (Kataoka et al. 2013). In addition, the field strength is around $3 \mu\text{G}$, and the energy density of the CRes is about 11% of that of the magnetic field, indicating a significant deviation from energy equipartition between the CRes and the magnetic field.

We also derived the confidence intervals of the CRe parameters beyond which the radio-fit conditions will never be met: $E_{br} \approx 3.5$ GeV for $p = 1.9$, 4–6 GeV for $p = 2.0$, and 6 GeV for $p = 2.1$ (Table 1). The radio conditions rule out the cases of $p \geq 2.2$ and $p \leq 1.8$. Thus, the possible range of e_{cre} would be $(3.4 - 6.0) \times 10^{-14} \text{ erg cm}^{-3}$.

The gamma-rays of the NPS are dominated by ICS on the starlight (SL; Figure 2). This is different from the Fermi bubbles, where most of the ICS signals below ~ 100 GeV come from the cosmic microwave background (CMB) in the leptonic model

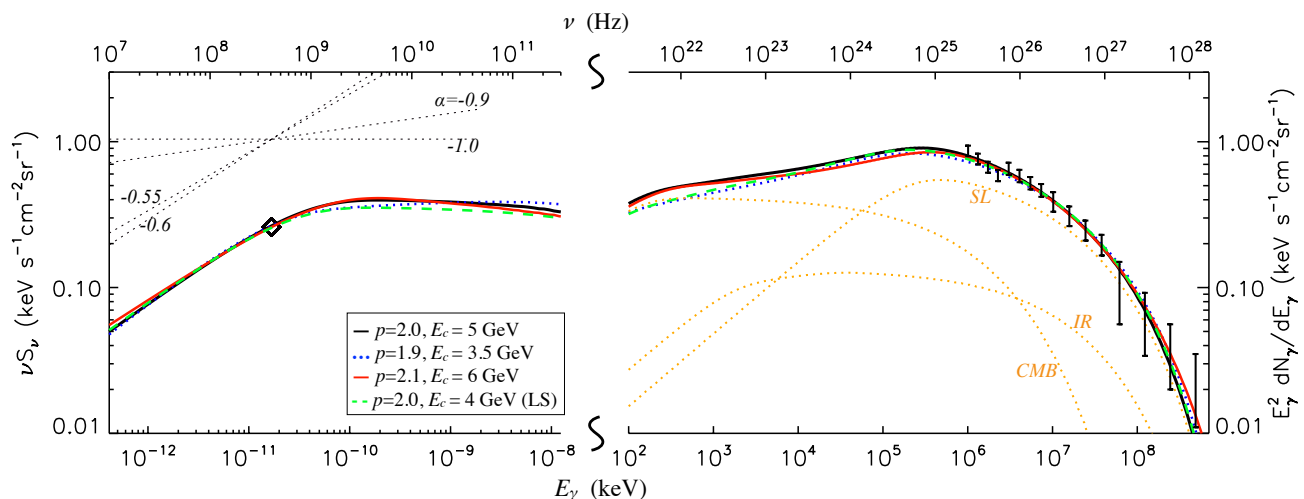


Fig. 2. Modeling the radio and gamma-ray spectra for the NPS. The diamond and error bars indicate the radio intensity (408 MHz) and gamma-ray data (Jóhannesson & Porter 2021) of the NPS, respectively. The dotted orange lines indicate the contributions of different components of the ISRF for $p = 2.0$ (see figure A1 for details).

(Ackermann et al. 2014) because the energy of CReS needs to exceed 300 GeV to generate GeV photons by scattering the CMB photons, and these electrons are quite rare in the NPS because the SED steepens above the cooling break energy E_{br} . Since the starlight dilutes with the height from the Galactic disk, this agrees with dimming of the gamma-ray NPS with latitude (e.g., Ackermann et al. 2014).

3. Discussion

According to X-ray observations, the post-shock gas accounting for the X-ray NPS has a temperature of 0.3 keV and a density of $n_{gas} \approx (3 - 4) \times 10^{-3} \text{ cm}^{-3}$ (Kataoka et al. 2015). Thus, the thermal pressure is $P_{th} \approx 3 \times 10^{-12} \text{ dyn cm}^{-2}$. The CRe acceleration efficiency of the shock in our fiducial case is $\eta_e \approx e_{cre} v_2 / \left[\frac{1}{2} \rho_1 v_s^3 (1 - C^{-2}) \right] = 1.8\%$, where C is the compression ratio, v_2 is downstream velocity, v_s is the shock velocity, and ρ_1 is the upstream density. This suggests that CReS can be efficiently accelerated by weak shocks. When the confidence intervals are considered, η_e would be (1–2)%.

This value is unusually high compared with the expectation of the canonical diffusive shock acceleration (DSA) theory given the low Mach number (e.g., $\lesssim 10^{-4}$ for Mach number $\lesssim 3$; Kang & Ryu 2013), but agrees with the speculation from observations of some radio relics. For these radio relics, the observed radio brightness suggests that η_e is probably very high (Kang et al. 2012; Brunetti & Jones 2014; Vazza et al. 2015; Botteon et al. 2020), which cannot be reconciled with the DSA mechanism (but see also Locatelli et al. 2020 for a radio relic consistent with DSA).

Moreover, the Mach number of 1.5 inferred from X-rays (Kataoka et al. 2013) is significantly lower than that deduced from DSA for $p < 2.2$ ($\mathcal{M} > 4.6$). Nevertheless, a similar case also arises in some radio relics where the X-ray derived Mach numbers are significantly lower than those inferred from radio spectra (see reviews by Brunetti & Jones 2014; van Weeren et al. 2019).

For the low Mach number, one could argue that, the electron temperature in the post-shock halo gas from X-rays might be lower than the ion temperature, and the Mach number might therefore be underestimated. Because of the high ion-to-electron

mass ratio, the post-shock ions (protons) are initially heated to $T_{p,0} \approx 3m_p v_s^2 / (4k_B C)$, where v_s is the shock speed, while electrons are heated to $T_{e,0} \approx T_{p,0} (m_e/m_p)$. Then, electrons gain energy while ions lose energy in Coulomb collisions. In the early period of this process, the ion temperature does not change significantly, and the evolution of the electron temperature (Spitzer 1962) can be simplified to

$$T_e(t) \approx \max \left[3.6 \times 10^5 \text{ K} \left(\frac{n_p}{1 \text{ cm}^{-3}} \frac{t}{1 \text{ yr}} \frac{T_{p,0}}{10^7 \text{ K}} \right)^{2/5}, T_{e,0} \right]. \quad (4)$$

The equipartition timescale between electrons and ions is $t_{eq} \approx 0.72 \text{ Myr} \left(\frac{T_{p,0}}{10^7 \text{ K}} \right)^{3/2} \left(\frac{n_p}{10^{-3} \text{ cm}^{-3}} \right)^{-1/3}$, while the dynamic timescale is $t_{dyn} \equiv R_{NPS} / v_s \gtrsim 15 \text{ Myr} \left(\frac{R_{NPS}}{10 \text{ kpc}} \right) \left(\frac{T_{p,0}}{10^7 \text{ K}} \right)^{-1/2}$, where R_{NPS} is the current size of the NPS. For the NPS with the X-ray-inferred temperature of 0.3 keV, we find that Coulomb collisions alone can efficiently heat electrons up to the temperature of ions, and thus the Mach number derived based on the thermal equilibrium is self-consistent.

We speculate that the high acceleration efficiency of CRe and flat radio spectra suggest that the CReS might be reaccelerated in the NPS. The CReS could have experienced multiple rounds of reacceleration by multiple weak shocks, and each reacceleration flattens the spectrum (Melrose & Pope 1993; Kang 2021). Observational signs of multiple bursts in the Galactic center over the past million years have been reported (Bland-Hawthorn et al. 2013; Bordoloi et al. 2017).

Nevertheless, there is another scenario according to which, the majority of CRe may have been accelerated by an evolving shock with a higher Mach number (e.g., $\mathcal{M} \geq 5$) in the early epoch, and transported to the current position, whereby the physics of the CReS is not related with the current Mach number. Given the enclosed mass of the halo medium ($M(r) \approx 1 \times 10^7 M_\odot r_{kpc}^{1.5}$; Miller & Bregman 2015), the radius of the evolving shock when $\mathcal{M} \geq 5$ is $\lesssim 0.2 R_{NPS} \approx 2 \text{ kpc}$ via the approximate relation that the shock energy $\sim M(R_s) \dot{R}_s^2 \sim \text{constant}$. From the conservation of mass, we derive that at present, the gas swept by a shock with $\mathcal{M} \geq 5$ constructs a 0.3 kpc shell

³ Accurate calculations show that the required time is $3.6 t_{eq}$ for the temperature difference between electrons and ions to fall within 10%.

adjacent to the contact discontinuity that is separated from the current shock front by the gas swept by that shock with a Mach number falling below 5 ($5 > M \geq 1.5$). The CRes within must diffuse through a thickness of several kiloparsecs to the current shock front. When we consider that the projected direction of the magnetic field basically traces the pattern of the NPS (Planck Collaboration 2016), the perpendicular diffusion coefficient in the evolving-shock picture probably is comparable to or exceeds the isotropic coefficient by several times $10^{28} \text{ cm}^2 \text{ s}^{-1}$ (Strong et al. 2007). Further discussion of this picture is beyond the current one-zone approximation in this Letter and is left for future work.

The cooling break energy of CRes (E_{br}) deduced from the radio and gamma-ray spectra is about 5 GeV. Given the ISRF energy density of $1.27 \times 10^{-12} \text{ erg cm}^{-3}$ at $(R, z) = (5 \text{ kpc}, 5 \text{ kpc})$ and the field strength of $3 \mu\text{G}$, the cooling timescale for CRes of 5 GeV is 60 Myr. When we adopt an ISRF energy density of $2.3 \times 10^{-12} \text{ erg cm}^{-3}$ near the midway of $(R, z) = (3 \text{ kpc}, 3 \text{ kpc})$, the cooling timescale would be shortened to 30–40 Myr. Thus, the cooling timescale of the cooling break energy agrees with the eROSITA bubble ages of 20 Myr (Predehl et al. 2020), suggesting that the results agree with the premise of the halo-structure nature.

For the LS scenario, the energy density of CRe we deduced is $(2 - 4) \times 10^{-12} \text{ dyn cm}^{-2}$. As a comparison, the pressure of the hot plasma of 10^6 Kelvin filling the local hot bubble is estimated to be $\sim 1 \times 10^{-12} \text{ dyn cm}^{-2}$ (Puspitarini et al. 2014; Snowden et al. 2014). The magnetic field measured by Voyager 1 when it crossed the heliopause is $\sim 5 \mu\text{G}$ (Burlaga & Ness 2014), while the estimate based on modeling of the radio emission in the Galactic plane is that the magnetic field at the position of the Sun is $\sim 3 \mu\text{G}$ (Jaffe et al. 2010). When we take the magnetic field of $5 \mu\text{G}$ as the representative value of the local bubble and assume that CRs and the magnetic field are in energy equipartition, the total pressure (including thermal pressure, magnetic pressure, and CRe pressure) of the local bubble is $\sim 3 \times 10^{-12} \text{ dyn cm}^{-2}$, which is close to the value in Cox (2005). Thus, the acceleration efficiency of the CRes in the LS scenario would be unusually high, which is a challenge for our current knowledge of the shock acceleration of SNRs. In addition, by integrating over the volume in the LS scenario (see the shell in Figure 1b, but scaled down 0.011 times), the total CRe energy exceeds 1×10^{50} erg. This value is also extraordinary compared with the 10^4 yr old SNRs Cygnus Loop and W44, whose total CRe energies derived from modeling the radio and gamma-ray data are $< 1 \times 10^{49}$ (Katagiri et al. 2011) and $\sim 10^{48}$ erg (Ackermann et al. 2013), respectively.

Acknowledgements. We thank the anonymous referee for insightful comments that improved our work. GM thanks Dr. Zhongqun Cheng and prof. Ruizhi Yang for helpful discussions. G.M. is supported by the National Program on Key Research and Development Project (Grants No. 2021YFA0718500, 2021YFA0718503), and NSFC (nos. 12133007 and 11833007).

References

Ackermann, M., Ajello, M., Allafort, A., et al. 2013, *Science*, 339, 807
 Ackermann, M., Albert, A., Atwood, W. B., et al. 2014, *ApJ*, 793, 64
 Aharonian F. A., 2004, *Very High Energy Cosmic Gamma Radiation: A Crucial Window on the Extreme Universe* (River Edge, NJ: World Scientific)
 Bell, A. R. 1978, *MNRAS*, 182, 443
 Bland-Hawthorn, J., Maloney, P. R., Sutherland, R. S., & Madsen, G. J. 2013, *ApJ*, 778, 58
 Bland-Hawthorn J., Gerhard O., 2016, *ARA&A*, 54, 529
 Blumenthal, G. R., & Gould, R. J. 1970, *Rev. Mod. Phys.*, 42, 237
 Bordoloi, R., Fox, A. J., Lockman, F. J., et al. 2017, *ApJ*, 834, 191
 Botteon A., Brunetti G., Ryu D., Roh S., 2020, *A&A*, 634, A64

Brunetti, G., & Jones, T. W. 2014, *Int. J. Mod. Phys. D*, 23, 1430007
 Burlaga, L. F., & Ness, N. F. 2014, *ApJ*, 784, 146
 Carretti, E., Crocker, R. M., Staveley-Smith, L., et al. 2013, *Nature*, 493, 66
 Casandjian, J. M., & Grenier, I. 2009, arXiv: 0912.3478
 Cox, D. P. 2005, *ARA&A*, 43, 337
 Das, K. K., Zucker, C., Speagle, J. S., et al. 2020, *MNRAS*, 498, 5863
 De Oliveira-Costa, A., Tegmark, M., Gaensler, B.M., et al. 2008, *MNRAS*, 388, 247
 Guo, F., & Mathews, W. G. 2012, *ApJ*, 756, 181
 Guzmán, A. E., May, J., Alvarez, H., & Maeda, K. 2011, *A&A*, 525, A138
 Haslam C. G. T., Salter C. J., Stoffel H., Wilson W. E., 1982, *A&AS*, 47, 1
 Jaffe, T. R., Leahy, J. P., Banday, A. J., et al. 2010, *MNRAS*, 401, 1013
 Jew, L., & Grumitt, R. D. P. 2020, *MNRAS*, 495, 578
 Jóhannesson, G., & Porter, T. A. 2021, *ApJ*, 917, 30
 Large, M. I., Quigley, M. J. S., Haslam, C. G. T., 1962, *MNRAS*, 124, 405
 Locatelli, N. T., Rajpurohit, K., Vazza, F., et al., 2020, *MNRAS*, 496, L48
 Kang, H. 2021, *J. Korean Astron. Soc.*, 54, 103
 Kang, H., Ryu, D. & Jones, T. W. 2012, *ApJ*, 756, 97
 Kang, H., & Ryu, D. 2013, *ApJ*, 764, 95
 Katagiri, H., Tibaldo, L., Ballet, J., et al. 2011, *ApJ*, 741, 44
 Kataoka, J., Tahara, M., Totani, T., et al. 2013, *ApJ*, 779, 57
 Kataoka, J., Tahara, M., Totani, T., et al. 2015, *ApJ*, 807, 77
 Miller, M. J., & Bregman, J. N. 2015, *ApJ*, 800, 14
 Melrose, D. B., & Pope, M. H. 1993, *PASA*, 10, 222
 Miville-Deschênes, M.-A., Ysard, N., Lavabre, A., et al. 2008, *A&A*, 490, 1093
 Moskalenko, I. V., Porter, T. A., & Strong, A. W. 2006, *ApJ*, 640, L155
 Mou, G., Yuan, F., Bu, D., et al. 2014, *ApJ*, 790, 109
 Mou, G., Sun, D., & Xie, F. 2018, *ApJ*, 869, L20
 Mou, G., Sun, D., Fang, T., et al. 2023, *Nature Communications*, 14, 781
 Panopoulou, G. V., Dickinson, C., Readhead, A. C. S., et al. 2021, *ApJ*, 922, 210
 Platania, P., Burigana, C., Maino, D., et al. 2003, *A&A*, 410, 847
 Planck Collaboration 2016, *A&A*, 594, A1
 Porter, T. A., Moskalenko, I. V., & Strong, A. W. 2006, *ApJ*, 648, L29
 Predehl, P., Sunyaev, R. A., Becker, W., et al., 2020, *Nature*, 588, 227
 Puspitarini, L., Lallement, R., Vergely, J. L., & Snowden, S. L. 2014, *A&A*, 566, A13
 Sarkar, K. C. 2019, *MNRAS*, 482, 4813
 Sironi L., Giannios D., 2013, *ApJ*, 778, 107
 Snowden, S. L., Egger, R., Freyberg, M. J., et al. 1997, *ApJ*, 485, 125
 Snowden, S. L., Chiao, M., Collier, M. R., et al. 2014, *ApJ*, 791, L14
 Sofue, Y. 1977, *A&A*, 60, 327
 Sofue, Y. 2000, *ApJ*, 540, 224
 Sofue, Y., 2015, *MNRAS*, 447, 3824
 Sofue, Y., Habe, A., Kataoka, J., et al. 2016, *MNRAS*, 459, 108
 Sofue, Y. 2019, *MNRAS*, 484, 2954
 Spitzer, L. 1962, *Physics of Fully Ionized Gases* (2nd ed.; New York: Interscience)
 Strong, A. W., Moskalenko, I. V., & Ptuskin, V. S. 2007, *Annu. Rev. Nucl. Part. Sci.*, 57, 285
 Su, M., Slatyer, T. R., & Finkbeiner, D. P. 2010, *ApJ*, 724, 1044
 van Weeren, R. J., de Gasperin, F., Akamatsu, H., et al. 2019, *SSRv*, 215, 16
 Vazza, F., Eckert, D., Brügggen, M., & Huber, B. 2015, *MNRAS*, 451, 2198
 Vidal, M., Dickinson, C., Davies, R. D., & Leahy, J. P. 2015, *MNRAS*, 452, 656
 Weaver, H. 1979, in *IAU Symp. 84, The Large-Scale Characteristics of the Galaxy*, ed. W. B. Burton (Dordrecht: Reidel), 295
 Wolleben, M. 2007, *ApJ*, 664, 349

Appendix A: Additional figure

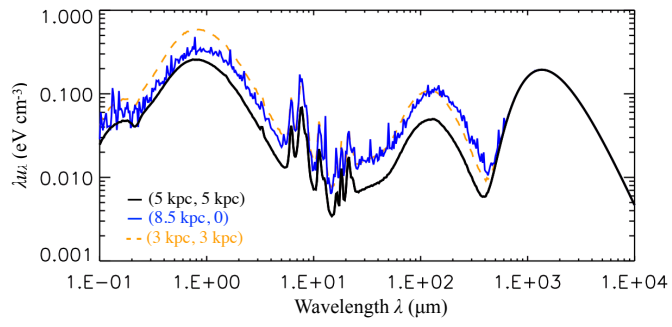


Fig. A1. ISRF at three different positions: $(R, z)=(5 \text{ kpc}, 5 \text{ kpc})$, $(8.5 \text{ kpc}, 0)$, and $(3 \text{ kpc}, 3 \text{ kpc})$. The three different components in the spectra are clearly visible: starlight, infrared light, and the CMB.